The coloring problem in intermetallics: bonding and properties of $Tb_3Zn_{3.6}Al_{7.4}$ with the La_3Al_{11} structure type

Mi-Kyung Han[I], Emilia Morosan[II], Paul C. Canfield[II] and Gordon J. Miller*,[I]

[I] Department of Chemistry, Iowa State University, Ames, Iowa 50011, USA
[II] Department of Physics & Astronomy, Iowa State University, Ames, Iowa 50011, USA

Dedicated to Professor Dr. Hans-Jörg Deiseroth on occasion of his 60th birthday

Received June 21, 2004; accepted August 4, 2004

Rare earth intermetallics / Chemical bonding / Magnetism / Single crystal structure analysis / Powder diffraction structure analysis / X-ray diffraction

Abstract. Single crystals of the new compound $Tb_3Zn_{3.6(1)}Al_{7.4(1)}$ were obtained from Al and Zn-rich ternary solutions. The title compound crystallizes in the orthorhombic La_3Al_{11} structure type (space group *Immm* (No. 71), $Z = 2$; $a = 4.2334(1)$ Å, $b = 9.9725(3)$ Å, $c = 12.4659(1)$ Å). The inverse susceptibility above ca. 50 K shows Curie-Weiss behavior, and a metamagnetic transition is apparent in the $T = 2$ K field-dependent magnetization around $H_c \approx 20$ kG. The resistivity increases with temperature in a roughly linear fashion, indicating the metallic character of this material. TB-LMTO-ASA electronic structure calculations indicate that this new intermetallic phase has all bonding states optimized in the $[Zn_{4-x}Al_{7+x}]$ network, which classifies this compound among the so-called "polar intermetallics." The calculations also provide a rationalization of the nonrandom ordering of Zn and Al atoms, which can be attributed to optimizing (Zn, Al)–(Zn, Al) orbital interactions.

Introduction

Polar intermetallics form a class of intermetallic compounds that are attracting increasing attention for studying chemical bonding between metals as well as for their potential physical properties [1–4]. There are at present no simple rules to identify such compounds in general, although the tendency is for an electropositive element, i.e., alkali, alkaline earth, or rare earth element, to combine with a molar excess of electronegative metals from among the late- and/or post-transition elements. Analysis of the theoretical electronic structure indicates that orbital interactions between the electronegative metals cross from bonding to antibonding at the Fermi level, which implies that metal-metal bonding within the electronegative framework is optimized [1]. The energy densities of states can show a pseudo-gap at the Fermi level, but this feature is not a prerequisite. If the minority electropositive component is among the rare earth elements, interesting physical properties are possible via the valence 4*f* orbitals, e.g., heavy fermion behavior [5]. Essentially, polar intermetallics are characterized by a robust partial structure of electronegative metal atoms with electropositive metals located in voids.

Among polar intermetallic structures, the tetragonal $BaAl_4$ structure type (also known as the $ThCr_2Si_2$-type) is the most prolific [6] and is particularly suited for placing rare earth elements into single tetragonally symmetric environments for studying the consequences of uniaxial magnetic anisotropy. $BaAl_4$-type tetra-aluminides with rare earth elements are reported for La–Sm [6], but these are characterized at elevated temperatures and are probably Al-deficient, i.e., $LnAl_{4-y}$, due to optimizing chemical bonding in the Al framework. At lower temperatures, the vacancies order into the La_3Al_{11} structure type [7]. One means to stabilize the $BaAl_4$ structure type with rare earth elements, then, is to substitute metals that are poorer in valence electrons than Al, e.g., Au or Zn, and these do exist, e.g., $LnAu_xAl_{4-x}$ (Ln: La–Tb; $0.75 \leq x \leq 2.00$) [8, 9]. As there are two distinct crystallographic sites for the electronegative metals in the $BaAl_4$ structure type, the distribution of two different elements introduces additional structural complexity, which is called the *coloring problem* [10]. Energetic factors controlling the site preferences for different elements in a structure can be separated into "site energies" and "bond energies." Moreover, exploration of this structure type reveals that it exists for 12–14 valence electrons assigned to the electronegative component [2, 11, 12]. With this flexibility in mind, we are studying rare-earth – zinc-aluminum phases, and in this report we report the synthesis, structure and properties of two new compounds in the Tb–Zn–Al system that form the La_3Al_{11} structure type.

* Correspondence author (e-mail: gmiller@iastate.edu)

Experimental

Synthesis

Single crystals of $Tb_3Zn_{4-x}Al_{7+x}$ ($x = 0.4$) were grown from high temperature ternary solutions, rich in Al and Zn [13–15]. These solutions were prepared from the pure elements, terbium (Materials Preparation Center, Ames Lab, 99.99% – metals analysis), aluminum ingots (Aesar 99.999%) and zinc ingots (Aesar 99.999%), in the molar ratio 10% Tb: 45% Zn: 45% Al. This (Al, Zn)-rich self-flux was chosen because it introduces no additional elements to the melt. The constituent elements were placed in an alumina crucible and sealed in a silica ampoule under a partial argon pressure. After initially heating the ampoule to above ca. 900 °C, it was cooled at 4 °C/hr to 650 °C. Subsequently, the excess solution was decanted as described in Ref. [13], and well-formed orthorhombic crystals were obtained. Their lengths were usually 2–5 mm, slightly more for a few larger crystals, whereas the cross-section varied from $\sim 1 \times 1\ mm^2$ (rods) to $\sim 1 \times 4\ mm^2$ (slabs). Powder X-ray diffraction on the different crystalline products confirmed that there is just a single phase product of $Tb_3Zn_{3.6(1)}Al_{7.4(1)}$.

Structure determination

The sample was characterized by single crystal and powder X-ray diffraction (XRD) techniques at ambient temperature. The powder diffraction pattern of the sample was obtained with a Huber image plate camera and monochromatic CuK_{α_1} radiation ($\lambda = 1.540598$ Å). Powdered samples were homogeneously dispersed on a Mylar film with the aid of a little petroleum jelly. The step size was set at 0.005° and the exposure time was 1 hr. Data acquisition was controlled via the in-situ program. In the X-ray powder pattern, only diffraction maxima expected for the corresponding $Tb_3Zn_{3.6(1)}Al_{7.4(1)}$ pattern were observed. The lattice parameters of $a = 4.2334(1)$ Å, $b = 9.9725(3)$ Å, $c = 12.4659(1)$ Å were obtained from least squares refinement with the aid of a Rietveld refinement program [16]. A block-like single crystal was selected from the product and was mounted on a Bruker APEX CCD-diffractometer equipped with monochromated MoK_α radiation ($\lambda = 0.71073$ Å), and diffraction data were collected at room temperature over a hemisphere of reciprocal space with 0.3° scans in ω and with an exposure time of 10 sec per frame up to $2\theta = 56.55°$. Intensities were extracted and then corrected for Lorentz and polarization effects using the SAINT program [17]. The program SADABS [18] was used for empirical absorption correction. Structure refinements (full-matrix least-squares on F^2) were performed using the SHELXTL package [19]. The crystallographic data are presented in Table 1; atomic coordinates and displacement parameters are listed in Table 2; selected interatomic distances are given in Table 3.

Table 1. Crystallographic data for $Tb_3Zn_{3.6(1)}Al_{7.4(1)}$.

Composition	$Tb_3Zn_{3.6}Al_{7.4}$
Temperature	293(2) K
Crystal size	$0.15 \times 0.15 \times 0.20\ mm^3$
Space group	*Immm* (No. 71)
Unit cell dimensions	$a = 4.2281(8)$ Å
	$b = 9.966(2)$ Å
	$c = 12.469(3)$ Å
Volume	525.38(18) Å^3
Z	2
Diffractometer	Bruker Apex
Wavelength	0.71073 Å (MoK_α)
2θ range for data collection	2.62 to 56.55°
Index ranges	$-5 \le h \le 5$, $-13 \le k \le 12$, $-16 \le l \le 12$
Reflections collected	1653
Independent reflections	389 [R(int) = 0.0838]
Completeness to $2\theta_{max}$	95.1%
Data/parameters	389/31
Goodness-of-fit on F^2	1.206
R indices (all data)	$R1^a = 0.0280$, $wR2^b = 0.0669$
Extinction coefficient	0.0244(10)
Largest diff. peak and hole	1.758 and −2.333 e$^-$ · Å^{-3}

a: $R1 = \sum ||F_o| - |F_c|| / \sum |F_o|$;
b: $wR2 = [\sum w(|F_o|^2 - |F_c|^2)^2 / \sum w|F_o|^4]^{1/2}$;
$w = 1/[\sigma^2(F_o^2) + (0.0244P)^2 + 1.4365P]$; $P = (F_o^2 + 2F_c^2)/3$

Table 2. Atomic coordinates, site occupation factors and isotropic temperature displacement parameters (in Å^2) for $Tb_3Zn_{3.6(1)}Al_{7.4(1)}$.

Atom	Site	x	y	z	Site Occ.		U_{iso} (Å^2)
Tb1	2a	0	0	0	1		0.007(1)
Tb2	4i	0	0	0.3146(1)	1		0.008(1)
M1	8l	0	0.3758(1)	0.3410(1)	0.73(1)	Zn	0.012(1)
					0.27	Al	
M2	4h	0	0.2104(3)	1/2	0.14(1)	Zn	0.011(1)
					0.86	Al	
M3	8l	1/2	0.2280(3)	0.3538(2)	0.09(1)	Zn	0.012(1)
					0.91	Al	
Al4	2d	1/2	0	1/2	1		0.011(1)

Table 3. Selected interatomic distances (Å) in $Tb_3Zn_{3.6(1)}Al_{7.4(1)}$ with frequency per formula unit indicated.

Atom–Atom	Distance (Å)	Atom–Atom	Distance (Å)
Tb1–M1	3.151(1) 8×	M1–M1	2.475(3) 2×
Tb1–M3	3.266(1) 4×	M1–M2	2.578(2) 4×
Tb1–M2	3.578(1) 4×	M1–M3	2.582(2) 8×
		M1–M3	2.640(2) 4×
Tb2–M2	3.121(2) 4×		
Tb2–M1	3.125(1) 8×	M2–M3	2.797(1) 8×
Tb2–Al4	3.132(1) 4×	M2–Al4	2.978(2) 4×
Tb2–M3	3.142(1) 8×		
Tb2–M3	3.429(1) 4×		
Tb2–M1	3.760(1) 4×	M3–Al4	2.913(3) 4×

Electronic structure calculations

Tight-binding, linear muffin-tin orbital (TB-LMTO) electronic structure calculations were carried out using the atomic sphere approximation (ASA) using the LMTO Version 47 program [20–23]. Exchange and correlation were treated in a local spin density approximation (LDA). All relativistic effects except spin-orbit coupling were taken into account using a scalar relativistic approximation.

Within the atomic sphere approximation (ASA), space is filled with small overlapping Wigner-Seitz (WS) atomic spheres. The radii of the WS spheres were obtained by requiring the overlapping potential to be the best possible approximation to the full potential according to an automatic procedure. The WS radii determined by this procedure are 3.774 Å for Tb, 2.712 Å for Zn and 2.940 Å for Al. The basis set included Tb 6*s*, 6*p*, 5*d* orbitals, Al 3*s*, 3*p*, and 3*d* orbitals and Zn 4*s*, 4*p* and 3*d* orbitals. The Tb 4*f* orbitals were treated as core functions occupied by eight electrons. The Löwdin downfolding technique allows the derivation of few-orbital effective Hamiltonians by keeping only the relevant degrees of freedom and integrating out the irrelevant ones. The **k**-space integrations to determine the self-consistent charge density, densities of states (DOS) and crystal Hamiltonian orbital populations (COHP) [24] were performed by the tetrahedron method. The Fermi level was chosen as an internal reference level in all cases.

Physical properties

Magnetization measurements on a plate-like crystal of $Tb_3Zn_{3.6}Al_{7.4}$ were performed in a Quantum Design MPMS SQUID magnetometer ($T = 1.8–350$ K, $H_{max} = 55$ kG), with $H = 1$ kG. The electrical resistance in zero field was measured with a Linear Research LR-700 AC resistance bridge ($f = 16$ Hz, $I = 1–3$ mA) in the magnetic field – temperature environment of the same QD MPMS system, using a standard four-probe technique. The heat capacity measurement was done in a Quantum Design PPMS system, using the relaxation technique and subtracting the sample holder and grease contribution, which were measured separately.

Discussion

Crystal structure of $Tb_3Zn_{3.6}Al_{7.4}$

$Tb_3Zn_{3.6}Al_{7.4}$ is a new compound adopting the La_3Al_{11} structure type at ambient temperature [7]. Its orthorhombic crystal structure is illustrated in Fig. 1 and emphasizes the coordination polyhedra surrounding the two distinct terbium atoms. Among the four crystallographic sites for the electronegative Zn and Al components (colored red or blue in Fig. 1), only the 2*d* site is fully occupied by Al atoms. These Al atoms are surrounded by eight (Zn, Al) atoms in a elongated square prism as well as four Tb atoms in a distorted square – the entire environment is closely related to the Al surroundings in cubic rare-earth trialuminides ($LnAl_3$) [6]. The other three sites (M1, M2 and M3) show mixed, yet nonrandom occupation by Zn and Al. Zn atoms strongly prefer the M1 (8*l*) sites (red spheres), which are coordinated by a pseudo-square pyramidal environment in the (Zn, Al) network. The axial direction shows a particularly short M1–M1 distance of 2.475(3) Å. Al atoms preferentially occupy the remaining two M2 and M3 sites. There are two types of polyhedra surrounding the terbium atoms (Fig. 1), which are distinguished by shaded and nonshaded yellow spheres. The Tb1 atoms (shaded yellow spheres) are coordinated by 16 Zn/Al atoms in an environment that closely resembles that of the Ba atoms in the $BaAl_4$ structure type. The Tb2 sites are encapsulated by 14 Al/Zn atoms at distances less than 3.5 Å with the coordination polyhedra completed by two M1 atoms at a distance of ca. 3.76 Å.

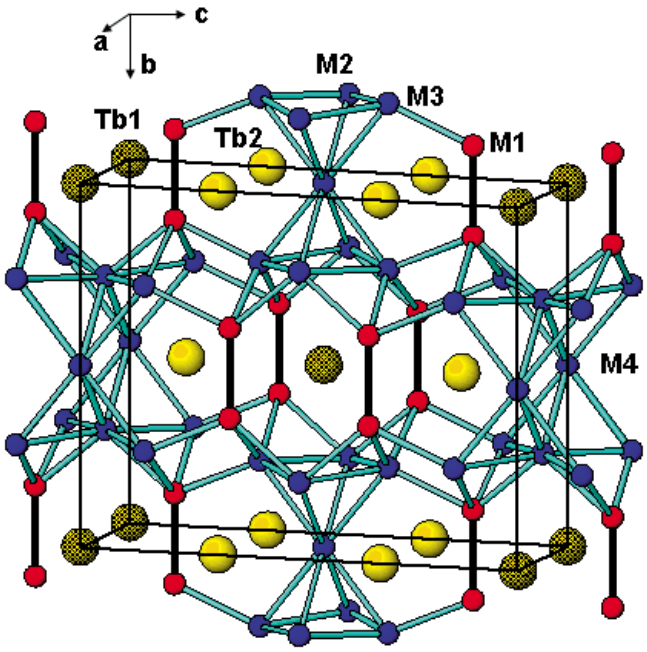

Fig. 1. Clinographic projection of orthorhombic $Tb_3Zn_{3.6(1)}Al_{7.4(1)}$ along the [100] direction and emphasizing the polyhedral surroundings of the Tb sites. Tb1: shaded yellow; Tb2: yellow; M1: red; M2–M4: blue spheres. Interatomic distances less than 2.50 Å: black; distances between 2.50 and 3.00 Å: light blue.

Electronic structure and bonding relationships

To understand the possible chemical bonding features influencing the stability of $Tb_3Zn_{3.6}Al_{7.4}$, TB-LMTO-ASA electronic structure calculations were performed on "$Tb_3Zn_4Al_7$" as the representative composition with the M1 site fully occupied by Zn atoms and the M2 and M3 sites fully occupied by Al atoms. The total DOS curve broken down into the different atomic contributions to the DOS as well as the COHP curve for all (Zn, Al)–(Zn, Al) contacts less than 3.00 Å in the $[Zn_4Al_7]$ network are shown in Fig. 2. The Fermi level, indicated by the dashed line, falls in the region of nonzero but low DOS, which, according to the accompanying COHP curve, corresponds to the energy region where (Zn, Al)–(Zn, Al) bonding levels crossover to antibonding levels. Therefore, metal-metal bonding within the electronegative part of the structure of "$Tb_3Zn_4Al_7$", on average, is optimized. Hence,

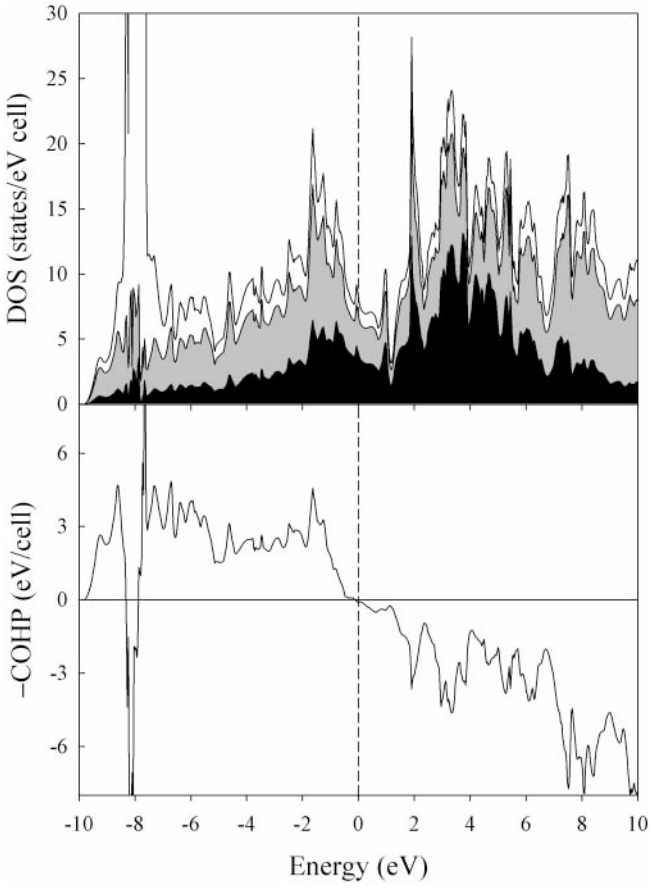

Fig. 2. (Top) Total DOS curve for "$Tb_3Zn_4Al_7$" separated into atomic contributions. Black: Tb; Gray: Al; White: Zn. (Bottom) Total COHP curve for all (Zn,Al)–(Zn,Al) contacts less than 3.00 Å in the $[Zn_4Al_7]$ network of "$Tb_3Zn_4Al_7$." The dashed line indicates the Fermi level.

$Tb_3Zn_{3.6}Al_{7.4}$ behaves like other "polar intermetallic" compounds, and the observed composition is significantly influenced by orbital interactions in the $[Zn_4Al_7]$ network. In fact, similar COHP analyses of "$(\ )_3Zn_4Al_7$", "Tb_3Al_{11}" and "$(\ )_3Al_{11}$" ("( )" means that the Tb site was treated as vacant in the calculation, i.e., contributing no orbitals to the set of valence orbitals in the structure) all give optimum metal-metal bonding near 38 valence electrons per formula unit, which exactly corresponds to "$Tb_3Zn_4Al_7$." A similar outcome was deduced for ternary rare-earth gold aluminides, $Ln_3Au_2Al_9$ [25]. COHP analyses of the specific orbital interactions in the $[Zn_4Al_7]$ network, shown in Fig. 3, indicate that the M1–M1 (Zn–Zn) interaction is optimized and Al–Al antibonding states are already occupied, while heteronuclear Zn–Al bonding states are not yet filled. Within a rigid band model, a few additional valence electrons can be accommodated into the electronic states of "$Tb_3Zn_4Al_7$" to optimize the heteronuclear Zn–Al interactions by replacing some Zn atoms with Al atoms: "$Tb_3Zn_{4-x}Al_{7+x}$."

To understand the site preference of Zn and Al atoms throughout the structure of $Tb_3Zn_{3.6}Al_{7.4}$, several different models of "$Tb_3Zn_4Al_7$" were constructed and their total energies were evaluated. To conduct this comparison, the Wigner-Seitz radii for Tb, Zn and Al, respectively, were kept constant for the different models. Table 4 lists the different models by identifying the Wyckoff sites (M1, M2

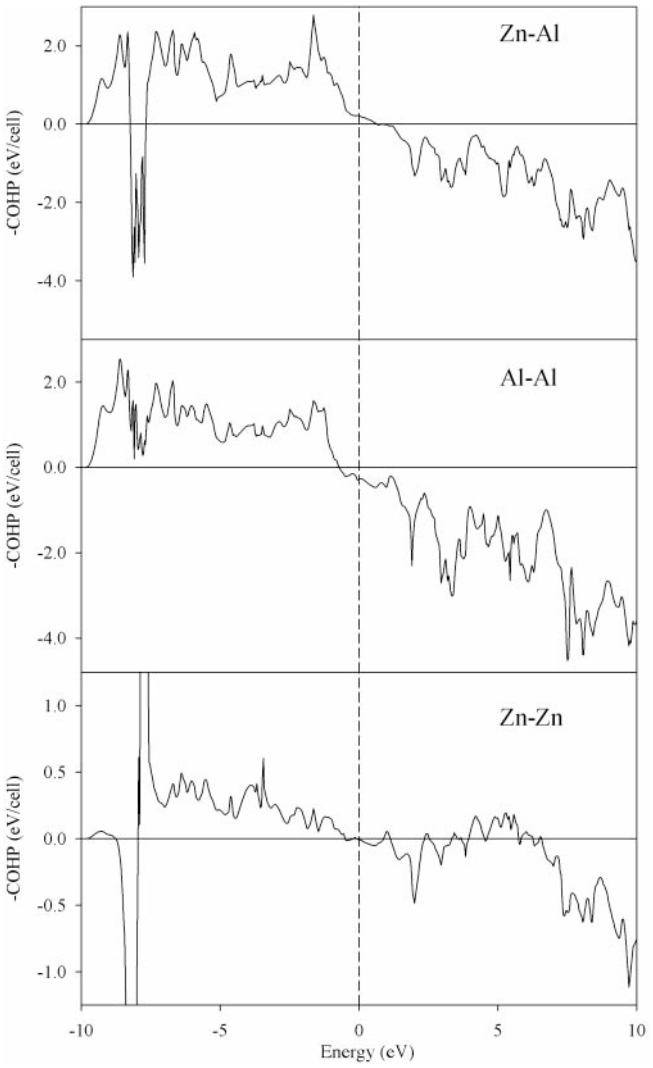

Fig. 3. COHP curves for (top) Zn–Al, (middle) Al–Al, and (bottom) Zn–Zn interactions less than 3.00 Å in the $[Zn_4Al_7]$ network of "$Tb_3Zn_4Al_7$." The dashed line marks the Fermi level. (–COHP values >0: bonding levels; –COHP values <0: antibonding levels.).

Table 4. Zn and Al distributions at M1, M2 and M3 sites and bond types in the $[Zn_4Al_7]$ network for six model structures of $Tb_3Zn_4Al_7$. Al atoms exclusively occupy the Al4 site (see Table 2).

	Models					
Sites	1 (*Immm*)	2 (*Immm*)	3 (*Pmmm*)	4 (*Pmmm*)	5 (*Pmmm*)	6 (*Imm*2)
M1 (8)	Zn	Al	$^1/_2$ Zn $^1/_2$ Al	$^1/_2$ Al	Al $^1/_2$ Zn	$^1/_2$ Zn $^1/_2$ Al
M2 (4)	Al	Al	Zn	Zn	Al	Al
M3 (8)	Al	Zn	Al	$^1/_2$ Zn $^1/_2$ Al	$^1/_2$ Al $^1/_2$ Zn	$^1/_2$ Zn $^1/_2$ Al
(eV/formula)	0	0.08	0.05	0.09	0.07	0.09
Bonds	Percentage with distances less than 2.50 Å (M1–M1 contacts)					
Al–Al	0	100	50	100	50	0
Zn–Al	0	0	0	0	0	100
Zn–Zn	100	0	50	0	50	0
	Percentage with distances more than 2.50 Å					
Al–Al	50	25	31.3	25	25	31.3
Zn–Al	50	75	62.5	62.5	62.5	62.5
Zn–Zn	0	0	6.2	12.5	12.5	6.2

and M3) occupied by the Zn and Al atoms. To include models that showed other distributions of Zn and Al atoms in the [Zn_4Al_7] network, the space group had to be modified to *Pmmm* or *Imm2* (NOTE: our study here is not exhaustive, but representative). In total, six different models were studied, and according to the relative total energies, Zn prefers to occupy the M1 (8*l*) sites, which is confirmed by our diffraction experiments. Table 4 also lists the percentages of Zn–Zn, Zn–Al and Al–Al interactions per unit cell for the M1–M1 pairs as well as the other contacts in the complete structure. In particular, when the M1 sites give the fewest number of homoatomic Al–Al contacts, the lowest energy arrangement is obtained, and the total energies increase linearly with the number of homoatomic Al–Al contacts. The corresponding COHP curves for the M1–M1 interactions for the different pairs of elements, shown in Fig. 4, indicate that Al–Al interactions have antibonding character, while Zn–Zn interactions have optimized bonding character at the calculated Fermi level. However, in "$Tb_3Zn_4Al_7$", the energy differences between the different structural models are small enough (i.e., 50–80 meV per formula unit) to assume that

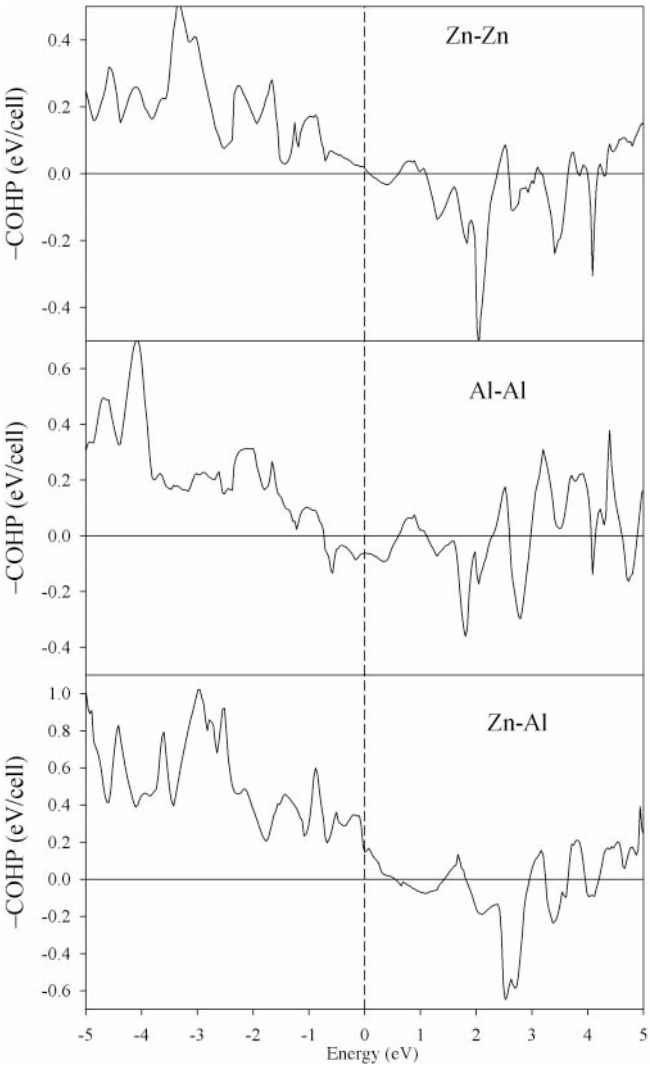

Fig. 4. M1–M1 ($d = 2.471$ Å) COHP curves for (top) Zn–Zn, (middle) Al–Al, and (bottom) Zn–Al contacts in various models of "$Tb_3Zn_4Al_7$." Dashed line indicates the Fermi level. (–COHP values >0: bonding levels; –COHP values <0: antibonding levels.).

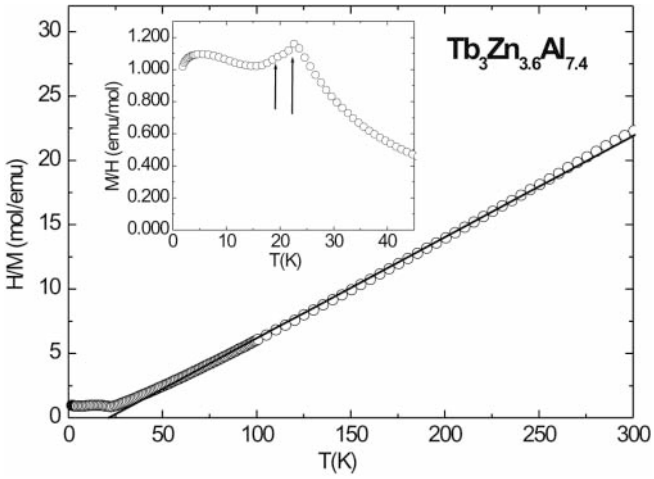

Fig. 5. Inverse susceptibility (open circles) and the linear Curie-Weiss fit for high temperatures (solid line); inset: low-temperature susceptibility with the arrows indicating the transition temperatures. The arrows indicate transition temperatures inferred from $\chi(T)$ as well as C_p(T) data shown in Fig. 7 (see text).

the influence of configurational entropy at elevated temperatures will favor a partially ordered arrangement of Zn and Al atoms, as is observed in the X-ray diffraction experiments. In the corresponding $Ln_3Au_2Al_9$, the "coloring problem" is dictated by eliminating Au-Au contacts, while the energies of the different configurations are significantly separated from the low energy configuration that there is no mixed occupancy observed other than at the M1 site [25].

Physical measurements

The temperature dependence of the inverse susceptibility (calculated as $1/\chi = H/M$) is shown in Fig. 5, whereas the inset presents the low temperature region of the susceptibility for the applied field $H = 1$ kG. The inverse susceptibility above ca. 50 K is consistent with Curie-Weiss behavior of the magnetization. A linear fitting of the inverse susceptibility in the paramagnetic state gives a value of the effective moment $\mu_{eff} = 9.86\mu_B$, which is close to the

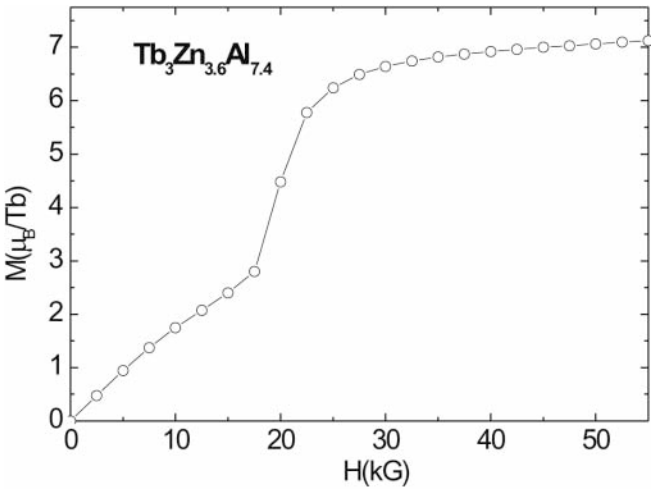

Fig. 6. Field dependent magnetization for $T = 2$ K and H up to 55 kG.

theoretical value for Tb^{3+} of 9.72 μ_B, and a value of θ_P, for this field orientation, of −29.7 K (using $\chi(T) = C/(T + \theta_P)$). The slightly enhanced effective moment may be due to small weighing error, or a consequence of its estimate based on a measurement along just one crystallographic direction. Anisotropic measurements would allow for an estimate of the polycrystalline average susceptibility, which we expect to give a more accurate value of μ_{eff}.

A magnetization measurement as a function of field is shown in Fig. 6 for the field directed along a face of a plate-like sample. One metamagnetic transition is apparent around $H_c \approx 20$ kG, leading to a magnetization of $7.1\mu_B$ at our maximum applied field of $H = 55$ kG, smaller than the saturated $9.0\mu_B$ calculated value. This is consistent with more metamagnetic transitions occurring above 55 kG, or with the Tb^{3+} magnetic moments being confined by the crystal electric field CEF to easy axes different from the main crystallographic directions. To verify the former hypothesis, measurements up to higher fields are required, whereas to address the latter assumption, at a minimum anisotropic magnetization measurements would be necessary.

The low temperature susceptibility for $H = 1$ kG (shown as an inset in Fig. 5) indicates antiferromagnetic ordering below the Néel temperature $T_N = 22.6$ K. This transition temperature, as well as a potential spin reorientation temperature can also be identified in the $d(\chi T)/dT$ (around 21.6 K and 18.6 K respectively) and $C_p(T)$ (at 22.5 K and 18.9 K, shown in Fig. 7). Based on all of the above measurements, we can summarize that the transition temperatures in $Tb_3Zn_{3.6}Al_{7.4}$ are $T_N = (22.05 \pm 0.45)$ K and $T_1 = (18.75 \pm 0.15)$ K.

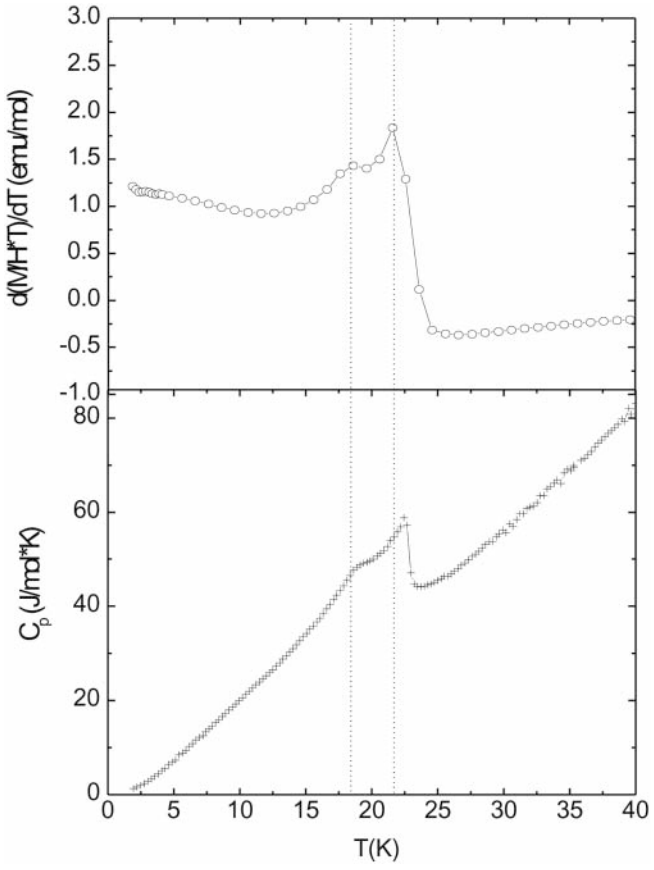

Fig. 7. Low-temperature (top) $d(\chi T)/dT$ and (bottom) heat capacity $C_p(T)$. The dotted lines mark the peak positions as determined from the top curve.

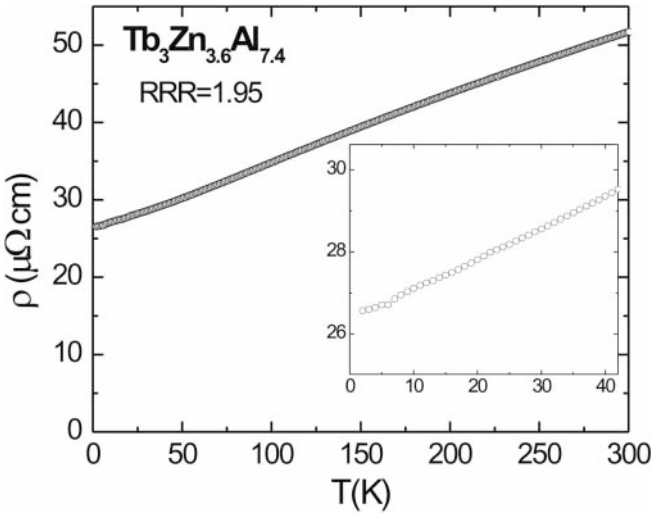

Fig. 8. Zero-field resistivity data (inset: enlarged low-temperature part).

The resistivity increases with temperature in a nearly linear fashion (Fig. 8), indicating the metallic character of this material. However, the large residual resistivity at $T = 2$ K ($\sim 26\ \mu\Omega \cdot$ cm) leads to a reduced residual resistivity ratio (RRR) of ca. 1.95, which is consistent with mixed (non-integral) site occupancies in this compound.

Conclusion

We have reported on a new intermetallic compound $Tb_3Zn_{3.6}Al_{7.4}$ that adopts the La_3Al_{11} structure type. Crystals suitable for both structural and property measurements were grown from an equimolar Zn : Al flux. Single crystal diffraction indicated that the Zn and Al atoms are partially ordered in this structure. Electronic structure calculations attribute the observed composition to optimizing metal-metal bonding in the electronegative (Zn, Al) framework, while the specific ordering is strongly influenced by specific orbital interactions, i.e., the bond-energy terms in the total electronic energy. Magnetic, calorimetric and resistivity measurements on $Tb_3Zn_{3.6}Al_{7.4}$ indicate metallic character with antiferromagnetically coupled Tb^{3+} sites, which show a metamagnetic transition in the field-dependent magnetization around $H_c \approx 20$ kG.

Acknowledgments. This work was supported by the NSF DMR 02-41092 and has been authored by Iowa State University of Science and Technology under Contract No. W-7405-ENG-82 with the U.S. Department of Energy. The authors thank Dr. S. L. Bud'ko for assistance in measuring magnetic susceptibilities, electrical resistivities and heat capacities.

References

[1] Miller, G. J.; Lee, C.-S.; Choe, W.: Structure and Bonding Around the Zintl Border. In: *Inorganic Chemistry Highlights*. (Eds. G. Meyer; D. Naumann; L. Wesemann) Wiley-VCH (2002) 21–53.

[2] Häussermann, U.; Amerioun, S.; Eriksson, L.; Lee, C.-S.; Miller, G. J.: The *s–p* Bonded Representatives of the Prominent

$BaAl_4$ Structure Type: A Case Study on Structural Stability of Polar Intermetallic Network Structures. J. Am. Chem. Soc. **124** (2002) 4371–4383.
[3] Amerioun, S.; Häussermann, U.: Structure and Bonding of Sr_3In_{11}: How Size and Electronic Effects Determine Structural Stability of Polar Intermetallic Compounds. Inorg. Chem. **42** (2003) 7782–7788.
[4] Lupu, C.; Downie, C.; Guloy, A.; Albright, T.; Mao, J.-G.: $Li_{17}Ag_3Sn_6$: A Polar Intermetallic π-System with Carbonate-like $[AgSn_3]^{11-}$ Anions and Trefoil Aromatic $[Ag_2Sn_3]^{6-}$ Layers. J. Am. Chem. Soc. **126** (2004) 4386–4397.
[5] Gout, D.; Benbow, E.; Gourdon, O.; Miller, G. J.: Theoretical Studies on Cerium Nickel Aluminides: Polar Intermetallics with Heavy Fermion Behavior. J. Solid State Chem. **176** (2003) 538–548.
[6] Villar, P.; Calvert, L. D.: Pearson's Handbook of Crystallographic Data for Intermetallic Phases, 2nd Ed. ASM International, Metals Park, OH, USA, 1991.
[7] Gomes de Mesquita, A. H.; Buschow, K. H. J.: The crystal structure of so-called α-$LaAl_4$ (La_3Al_{11}). Acta Crystallogr. **22** (1967) 497–501.
[8] Hulliger, F.: On Rare Earth Gold Aluminides $LnAuAl_3$ and Related Compounds. J. Alloys Comp. **218** (1995) 255–258.
[9] Hulliger, F.; Nissen, H.-U.; Wessicken, R.: On New $CaBe_2Ge_2$-type Representatives MAu_2Al_2. J. Alloys Comp. **206** (1994) 263–266.
[10] Miller, G. J.: The "Coloring Problem" in Solids: How It Affects Structure, Composition and Properties. Eur. J. Inorg. Chem. (1998) 523–536.
[11] Zheng, C.; Hoffmann, R.: An Unusual Electron Count and Electron-Deficient Multi-Center Bonding in One Class of Intermetallics. The Barium–Aluminum ($BaAl_4$), Calcium–Aluminum–Zinc ($CaAl_2Zn_2$), Cerium–Magnesium–Silicide ($CeMg_2Si_2$) and fcc Al Structures. Z. Naturforsch. B**41** (1986) 292–320.
[12] Burdett, J. K.; Miller, G. J.: The Fragment Formalism in Main Group Solids: Applications to AlB_2, $CaAl_2Si_2$, $BaAl_4$, and Related Materials. Chem. Mater. **2** (1990) 12–26.
[13] Fisk, Z.; Remeika, J. P.: Handbook of Physics and Chemistry of Rare Earths, 12 (Eds. Gschneidner, K. A.; Eyring, L. R.), North-Holland, Amsterdam (1989) p. 5.
[14] Canfield, P. C.; Fisk, Z.: Growth of single crystals from metallic fluxes. Philos. Mag. B **65** (1992) 1117–1.
[15] Canfield, P. C.; Fisher, I. R.: High-temperature solution growth of intermetallic single crystals and quasicrystals. J. Crystal Growth **225** (2001) 155–161.
[16] Hunter, B. A.; Howard, C. J. Rietica; Australian Nuclear Science and Technology Organization: Menai, Australia (2000).
[17] SMART; Bruker AXS, Inc.; Madison, WI (1996).
[18] Blessing, R. H.: An empirical correction for absorption anisotropy. Acta Crystallogr. A**51** (1995) 33–38.
[19] SHELXTL; Bruker ASX, Inc.: Madison, WI, (2000).
[20] Tank, R. W.; Jepsen, O.; Burckhardt. A.; Andersen, O. K.: TB-LMTO-ASA Program, Vers. 4.7; Max-Planck-Institut für Festkörperforschung: Stuttgart, Germany (1998).
[21] Skriver, H. L.: The LMTO Method. Springer-Verlag: Berlin, Germany (1984).
[22] Jepsen, O.; Sob, M.; Andersen, O. K.: Linearized Band-Structure Methods in Electronic Band-Structure and its Applications; Springer Lecture Note. Springer-Verlag: Berlin, Germany (1987).
[23] Andersen, O. K.; Jepsen, O.: Explicit, First-Principles Tight-Binding Theory. Phys. Rev. Lett. **53** (1983) 2571–2574.
[24] Dronskowski, R.; Blöchl, P.: Crystal orbital Hamilton populations (COHP): energy-resolved visualization of chemical bonding in solids based on density-functional calculations. J. Phys. Chem. **97** (1993) 8617–8624.
[25] Nordell, K. J.; Miller, G. J.: $Ln_3Au_2Al_9$ (Ln = Dy, Tb): Heteronuclear versus Homonuclear Bonding in Intermetallic Phases. Angew. Chem. Int. Ed. Engl. **36** (1997) 2008–2010.